

Confinement property of tracer impurity particle inside a static magnetic island O-point of Large Helical Device

Naoki TAMURA, Yi LIU¹⁾, Naofumi IWAMA²⁾, Shigeru SUDO,
Konstantin V. KHLOPENKOV, Artem Yu. KOSTRIOUKOV, Byron J. PETERSON,
Shigeru INAGAKI, Yoshio NAGAYAMA, Kazuo KAWAHATA, Tomohiro MORISAKI,
Katsumi IDA, Nobuyoshi OHYABU, Akio KOMORI and LHD Experimental Group

National Institute for Fusion Science, Toki 509-5292, Japan

¹⁾*South-Western Institute for Physics, 432, Chengdu 610041, China*

²⁾*Daido Institute of Technology, Nagoya 457-8530, Japan*

(Received: 30 August 2008 / Accepted: 20 January 2009)

By using tracer-encapsulated solid pellet injection, the local deposition of tracer impurity particle is achieved only inside a $n/m = 1/1$ static magnetic island O-point produced by external perturbation coils in the Large Helical Device (LHD). In LHD, two 20-channel AXUV diode arrays have been installed on a semi-tangential cross-section to obtain a 2D computed tomography image of the plasma radiation. The reconstructed tomography image indicates that the radiation from the tracer impurity deposited inside the O-point of the $n/m = 1/1$ island is extremely localized and remains inside the island for a comparatively long time. This experimental result clearly indicates that the confinement capability of the impurity particle inside the O-point of the $n/m = 1/1$ island is better than that outside the island.

Keywords: magnetic island, impurity transport, tracer-encapsulated solid pellet, LHD

1. Introduction

Observations of internal transport barriers at or near a rational magnetic surface in magnetically-confined plasmas [1, 2] create interest in the roles of a magnetic island in the plasma confinement. Beside that, properties, such as transport, inside the magnetic island itself have come to be also important issues to be clarified. Various experiments in many tokamaks and helical devices have revealed the properties of heat and particle transport in the static magnetic island so far. The observations of flat profiles of various plasma parameters, such as electron temperature [3], electron density [4], and ion temperature [5], inside the magnetic island are the most prominent results in those experiments. The flattening inside the magnetic island itself does not support a high transport level of heat and particles inside the island, since the energy and particle balance in the island is considered to be highly isolated from the ambient plasmas [6]. External perturbation experiments with pellet injection have offered new insight into the transport inside the island. In JET, low particle diffusivity inside the magnetic island is suggested by the resulting "snake" oscillation after the D_2 pellet injection [7, 8]. In the Large Helical Device (LHD), clear evidence for a reduction of heat transport inside the $n/m = 1/1$ magnetic island O-point (electron heat diffusivity inside the island, $0.2 \text{ m}^2/\text{s}$, is an order of magnitude less than that outside the island) is observed from a cold pulse propagation induced by a tracer-encapsulated solid pellet (TESPEL) [9]. However, no clear experi-

mental investigation on impurity transport inside the magnetic island has been reported so far, although the attendant impurity accumulation inside the island has been observed in PBX [10] and JET [8]. In this paper, the achievement of the local deposition of tracer impurity only inside the $n/m = 1/1$ static magnetic island O-point and the observation of the low transport level of the tracer impurity inside the island O-point are presented.

2. Experimental results

The LHD is a heliotron-type magnetic confinement fusion device, which has 10 pairs of external perturbation coils, so-called Local Island Divertor (LID) coils [11]. The LID coils enables us to control the size of the $n/m = 1/1$ magnetic island by changing the perturbation coil current, I_{LID} . In order to introduce a tracer impurity inside the $n/m = 1/1$ magnetic island O-point, TESPEL [12] injection is used. Briefly speaking, TESPEL is a double-layered impurity pellet, which consists of polystyrene polymer ($-\text{CH}(\text{C}_6\text{H}_5)\text{CH}_2-$) as an outer shell (the typical diameter ranges from 0.4 mm to 0.9 mm) and tracer particles as an inner core (the typical size is $0.05 \sim 0.2 \text{ mm}$ in size). This structure of the TESPEL enables us to achieve the local deposition of tracer impurity inside the plasma. Figure 1(b) shows the successful example of the local deposition of tracer impurity inside the $n/m = 1/1$ magnetic island O-point with the TESPEL injection [13]. In this instance, a magnetic axis position of R_{ax} and a magnetic field at the axis B_{ax} are 3.5 m and 2.976 T, respectively. And I_{LID} of -1200 A is

author's e-mail: ntamura@LHD.nifs.ac.jp

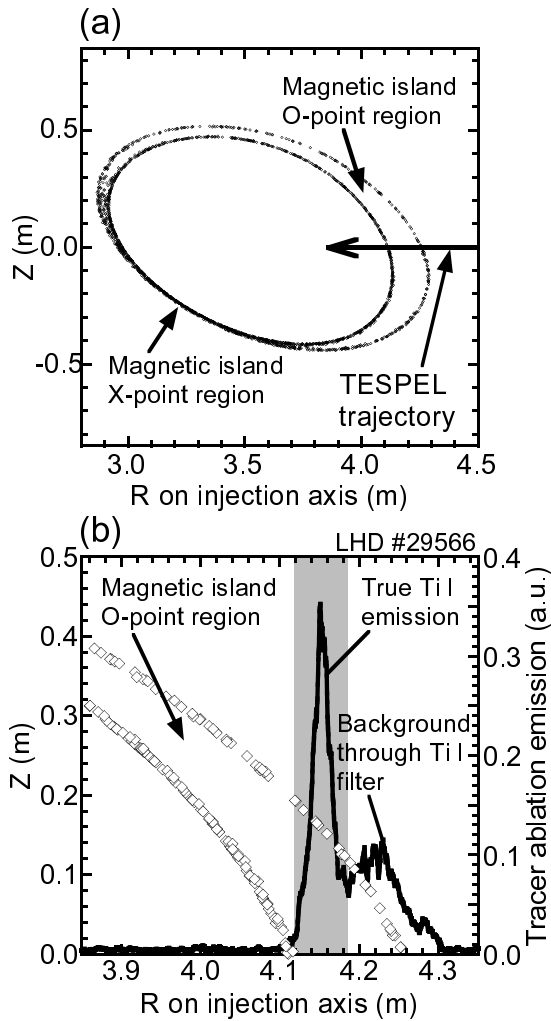


Fig. 1 (a) Poloidal cross-section of a $n/m = 1/1$ magnetic island produced by external perturbation coils. In this case, the O-point of the $n/m = 1/1$ magnetic island is placed on the TESPEL injection axis. (b) Tracer ablation emission measured with photomultipliers equipped with an Ti I filter (solid line) as a function of the major radial position along the TESPEL injection axis. Here, the O-point of the $n/m = 1/1$ magnetic island is the region enclosed by open diamond symbols.

applied in order to expand the width of the $n/m = 1/1$ magnetic island O-point along the TESPEL injection axis (~ 14 cm), as shown in Fig. 1(a). The TESPEL parameters are as follows: the outer diameter is 0.42 mm, the resulting velocity is 324 m/s and the tracer consists of three titanium (Ti) balls (which diameter are 0.06 mm, 0.08 mm and 0.1 mm, respectively). The line-averaged electron density and the central electron temperature just before the TESPEL injection are $1.0 \times 10^{19} \text{ m}^{-3}$ and 2.6 keV, respectively. The most delicately adjusted parameters in this experiment are the outer diameter of the TESPEL and the electron temperature of the target plasma to control precisely the

location of the tracer deposition. A very sharp peak of the solid line in Fig. 1(b) represents the deposited location of the Ti tracer, which is within the $n/m = 1/1$ magnetic island O-point region enclosed by open diamond symbols. This boundary of the $n/m = 1/1$ magnetic island shown in Fig. 1(b) is calculated under vacuum conditions. Since the ratio of the plasma pressure to the magnetic pressure in this discharge is estimated as only 0.09 % by the magnetic diagnostics, the calculated boundary for the vacuum can still be applicable for this case. The end of the tracer ablation within the region of the $n/m = 1/1$ magnetic island O-point is also confirmed by ECE diagnostics.

In order to observe the spatio-temporal behavior of the tracer impurity deposited inside the O-point of the $n/m = 1/1$ island, two 20 channel Absolute eXtreme UltraViolet photoDiode (AXUVD) arrays [14], which have been installed on a semi-tangential cross-section of LHD [15], are used. Figure 2(a) shows the positional relationship between the TESPEL injection axis and the semi-tangential cross-section with the AXUVD arrays. The AXUVD array has been utilized widely for the plasma radiation measurement in the various magnetically-confined plasma experiments [16, 17, 18]. The AXUVD has a stable and high quantum efficiencies for XUV photons, compared with conventional XUV detectors. And the advantage of the AXUVD array over the conventional foil bolometer is that it has a considerably higher temporal resolution (it can be on the μs time scale, but in LHD it is down to $100 \mu\text{s}$ due to the capacity of the A/D converter) and no sensitivity for neutrals. The AXUVD arrays used here are un-filtered and thus can observe the plasma radiation, whose energy is ranged from 1.1 eV to 6000 eV, although the quantum efficiency loss exists in the low energy region (for 7 eV to 100 eV photons). Figure 2(b) shows the layout of the lines of sight of the AXUVD arrays with the LHD vacuum vessel for this experiment. The AXUVD measurement of the tracer impurity deposited inside the $n/m = 1/1$ magnetic island O-point is performed with $R_{\text{ax}} = 3.6$ m, $B_{\text{ax}} = 2.75$ T. The I_{LID} of -1920 A is applied to expand the width of the $n/m = 1/1$ magnetic island O-point along the TESPEL injection axis. In Fig. 2(b), the shape of the $n/m = 1/1$ magnetic island under the above magnetic configuration is also shown. Figure 3 shows the temporal evolution of the vertical AXUVD (STU) array signal around the time of the TESPEL (with the Ti tracer) injection toward the O-point of the $n/m = 1/1$ island. Channel number 14 of the STU array sees strongly the region where the TESPEL plume is expected to appear. As a reference, the injection of TESPEL without the Ti tracer toward the O-point of the $n/m = 1/1$ island is performed with the same I_{LID} and the injection of TESPEL with the Ti tracer across the X-point (outside the O-point)

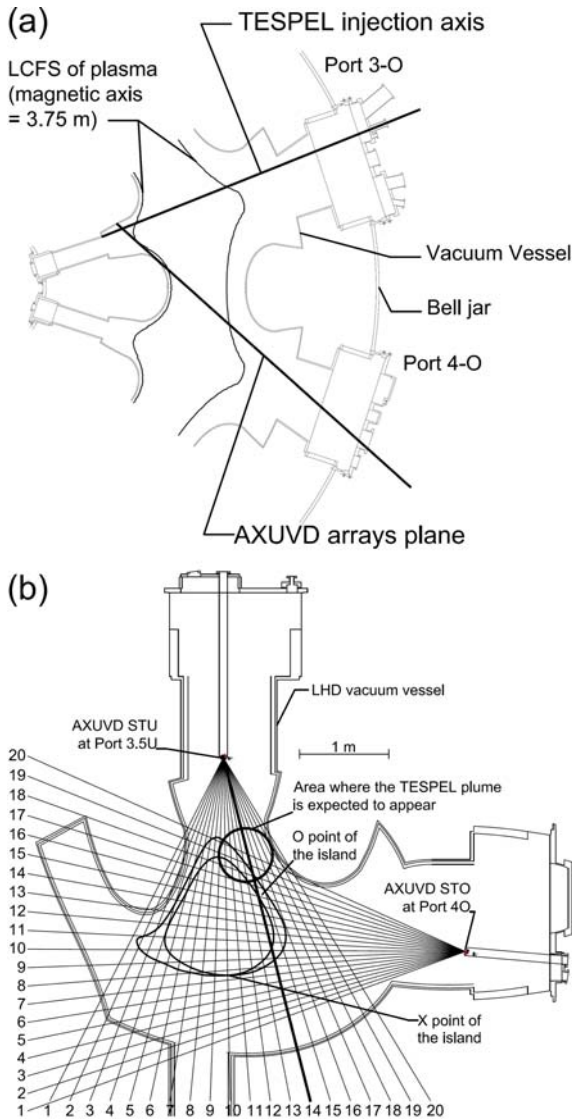


Fig. 2 (a) Partial equatorial plane view of LHD with the TESPEL injection axis. The line of intersection of an AXUVD arrays plane with the equatorial plane is also shown. (b) Layout of two 20 ch. AXUVD arrays on the semi-tangential cross-section of LHD. The shape of the $n/m = 1/1$ magnetic island is also depicted. In this case, the O-point of the island exists on the TESPEL injection axis. The area where the TESPEL plume is expected to appear is circled with a thick solid line.

of the $n/m = 1/1$ island is performed with the I_{LID} value of +1920 A. In the case of the TESPEL injection across the X-point of the $n/m = 1/1$ island, the essential parameters for the case of the TESPEL injection across the X-point of the $n/m = 1/1$ island have maintained and only the $n/m = 1/1$ island O-point region is removed from the TESPEL injection axis by changing both the current of external perturbation coils and its polarity. The temporal behaviors of the STU array signals for those cases are also plot-

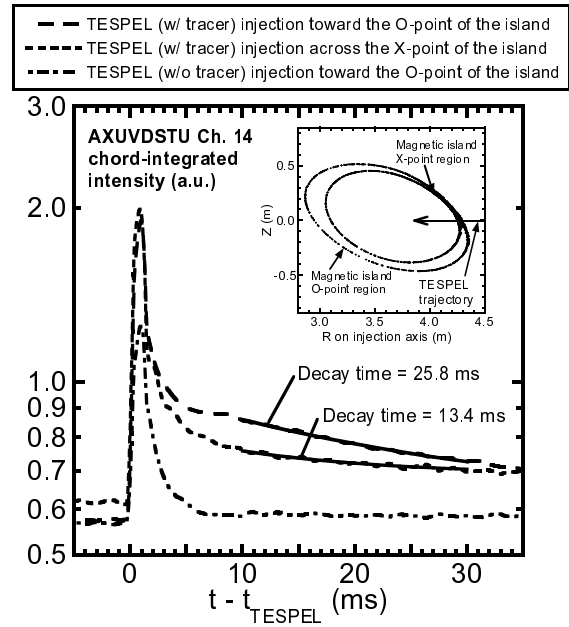


Fig. 3 Temporal evolution of the AXUVD signal around the time of the TESPEL (with the Ti tracer) injection toward the O-point of the $n/m = 1/1$ magnetic island (long-dashed line). As a reference, the cases of the TESPEL (with the Ti tracer) injection across the X-point of the island (short-dashed line) and the TESPEL (without the Ti tracer) injection toward the O-point of the island (dashed-dotted line) are also plotted. Channel number 14 of the STU array sees strongly the region where the TESPEL plume is expected to appear. The plasma and TESPEL parameters are almost the same in all the cases. Decay times of the AXUVD signal shown in the figure are evaluated from the time period of $t - t_{TESPEL}$, 10 ms to 30 ms and the evaluated decay curves are indicated by solid lines. Poloidal cross-section of the $n/m = 1/1$ magnetic island for the case of TESPEL injection across the X-point of the island is displayed in the figure.

ted in Fig. 3. The unit of the STU signals is an arbitrary unit, since our AXUVD system is not calibrated for the absolute radiation measurement. The plasma and TESPEL parameters are almost the same in all the cases. As can be seen in Fig. 3, just after the TESPEL injection, all AXUVD signals are increased and decreased promptly. This very sharp peak can be attributed to both the shell and tracer plume, because a typical time for TESPEL ablation in LHD is about 1 ms [19]. The subsequent decay curve of the AXUVD signals is mainly due to the radiation from the carbon impurity from the outer shell for the case without the tracer and the tracer impurity for the case with the tracer. In the case of the injection of TESPEL with the Ti tracer toward the O-point of the island, the decay time of the signal intensity from the channel 14 of the STU array is evaluated to be 25.8 ms from the

time period of $t - t_{\text{TESPEL}}$, 10 ms to 30 ms. In the case of the injection of TESPEL with the Ti tracer across the X-point of the island, the decay time is evaluated to be 13.4 ms for the same time period (In Fig. 3, solid lines indicate fitted decay curves). Thus this suggests that the tracer impurity deposited inside the $n/m = 1/1$ magnetic island O-point remains in the island for a comparatively long time, taking into account the difference in the confinement volumes.

3. 2D CT analysis for the radiation from the tracer

In order to have a clear understanding of the behavior of the radiation from the tracer impurity inside the $n/m = 1/1$ magnetic island O-point, 2D computed tomography (CT) analysis is applied for the measured chord-integrated AXUVD signals. In this analysis, the semi-tangential cross-section including all the lines of sight of AXUVD arrays shown in Fig.2(b) is divided by $32 \times 32 = 1024$ pixels.

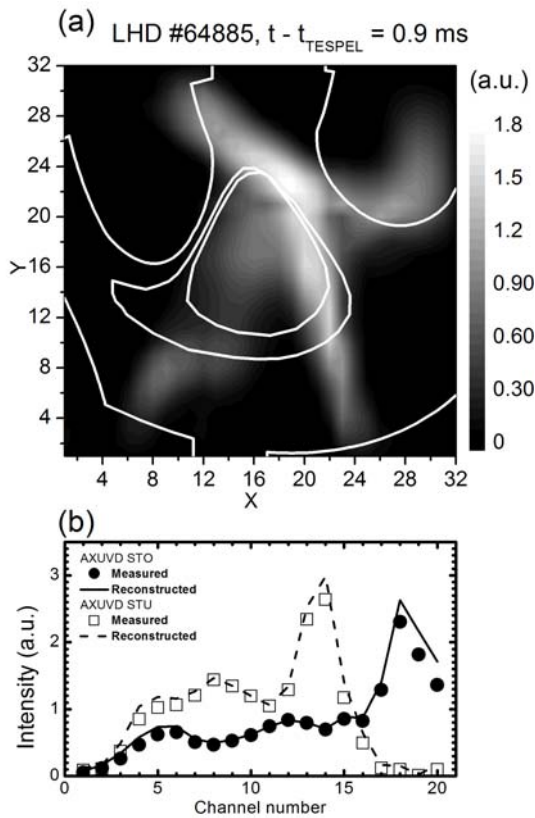


Fig. 4 (a) Example of the reconstructed 2D CT image of AXUVD signals for the case of the TESPEL injection across the X-point of the $n/m = 1/1$ island. The vacuum vessel of LHD and the shape of the expanded $n/m = 1/1$ magnetic island are depicted by white lines in the image. (b) Comparison of the data between measured (symbols) and reconstructed (lines) from both vertical AXUVD (STU) array and horizontal AXUVD (STO) array.

Since the number of image cells extremely exceeds the number of the detector channels, $M = 20 + 20 = 40$, the reconstruction of 2D CT image is a well-known ill-posed problem. To solve this problem, a linear (Phillips-Tikhonov) regularization method [20] is used. The reconstructed image is formed by minimizing the quantity $J \equiv \gamma \|C\mathbf{E}\|^2 + (1/M)\|\mathbf{S} - L\mathbf{E}\|^2$, where the γ is the reciprocal of the Lagrangian multiplier and the C is the Laplacian matrix. \mathbf{E} and \mathbf{S} are the vectors containing local intensities of radiation and detector signals, respectively. L is the geometric weighting matrix. The γ can act on the smoothness of the reconstructed image. In addition to Phillips-Tikhonov regularization, a technique based on the minimum Fisher information principle [21] is also utilized. This technique allows us to avoid the oversmoothing of the peak in the reconstructed CT image and to decrease the peripheral artifacts in the reconstructed CT images. Further details about the applied CT analysis technique are described in [22]. Figure 4(a) shows the example of the reconstructed 2D CT image of AXUVD signals. The image is obtained just after the TESPEL injection ($t - t_{\text{TESPEL}} = 0.9$ ms) in the case of the injection of TESPEL with the Ti tracer across the X-point of the $n/m = 1/1$ island. As can be clearly seen, a highly-localized radiation exists in the upper right region of the 2D CT image. This region corresponds to the region where the TESPEL plume can appear. Since the typical time for the TESPEL ablation is about 1 ms, this intense radiation can be attributed to the light emissions from both the shell and tracer plume. However, in the 2D CT image, two bright lines extending from a bright spot can be recognized (one line to the diagonally upper left region and the other line to the lower region). These lines seem not to be spread along the magnetic field lines. And there exists an emitting region outside the LHD vacuum vessel. Unfortunately, those are artifacts of the tomographic reconstruction process. Nevertheless, the reconstruction of the 2D CT image with such highly asymmetric patterns is almost achieved since the reconstructed AXUVD signals for both the vertical and horizontal array agree well with the measured ones, as shown in Fig. 4(b).

Figure 5 shows the reconstructed 2D CT images of AXUVD signals just before and after the injection of TESPEL with the Ti tracer toward the O-point of the $n/m = 1/1$ island. The 2D radiation profile just before the TESPEL injection shows the almost center-peaked one and it is changed drastically with the injection of the TESPEL. At the time of $t - t_{\text{TESPEL}} = 1.8$ ms, as shown in Fig. 5(c), it is recognized that intense radiation can be seen inside the O-point of the $n/m = 1/1$ island. This intense radiation region is still found inside the O-point of the $n/m = 1/1$ island at the time of $t - t_{\text{TESPEL}} = 2.8$ ms (see Fig. 5(d)). And sur-

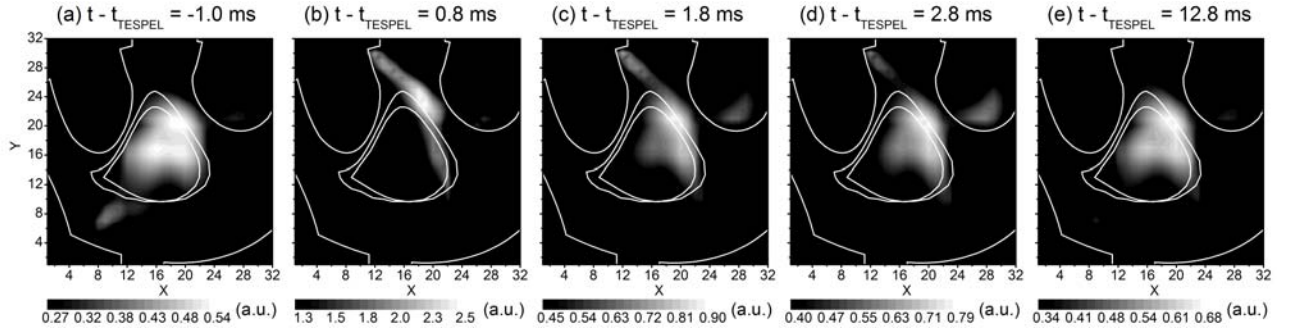


Fig. 5 Reconstructed CT images for the case with the injection of TESPEL with the Ti tracer toward the O point of the $n/m = 1/1$ island. (a) just before the injection ($t - t_{\text{TESPEL}} = -1.0$ ms), (b) 0.8 ms, (c) 1.8 ms, (d) 2.8 ms and (e) 12.8ms after the injection. The vacuum vessel of LHD and the $n/m = 1/1$ magnetic island are also displayed by white lines in the images.

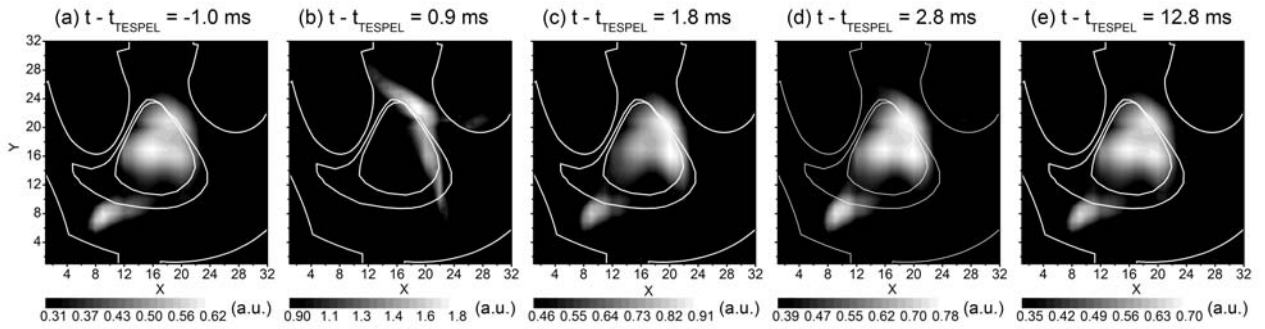


Fig. 6 Reconstructed CT images for the case with the injection of TESPEL with the Ti tracer across the X point of the $n/m = 1/1$ island. (a) just before the injection ($t - t_{\text{TESPEL}} = -1.0$ ms), (b) 0.9 ms, (c) 1.8 ms, (d) 2.8ms and (e) 12.8 ms after the injection.

prisingly, even an additional ten ms later ($t - t_{\text{TESPEL}} = 12.8$ ms as shown in Fig. 5(e)), the radiation from inside the island O-point is still stronger than that outside the island O-point. In this case, the original shape of the 2D radiation profile is finally restored after a time of around $t - t_{\text{TESPEL}} = 15$ ms. In the case with the tracer impurity deposited outside the O-point of the $n/m = 1/1$ island (TESPEL with the Ti tracer has injected across the X-point of the $n/m = 1/1$ magnetic island), as can be seen in Fig. 6(b), the highly-localized radiation due to the TESPEL injection exists in the same manner as in Fig. 5(b). However, the original shape of the profile is rapidly recovered at the time of $t - t_{\text{TESPEL}} = 2.8$ ms. Thus the 2D CT analysis clearly suggests that the tracer impurity deposited inside the O-point of the $n/m = 1/1$ island is well-confined for a comparatively long time.

4. Discussions

In the case shown in Fig. 5, the dominant charge state of the titanium tracer ions, which are introduced inside the $n/m = 1/1$ magnetic island O-point by

TESPEL injection, is estimated to be around +15 by using the calculation code, MIST [23]. Accordingly the finite orbit width of the titanium tracer ions inside the $n/m = 1/1$ magnetic island O-point is estimated as less than 1 cm on the assumption that the temperature of titanium tracer ions is the same as the electron temperature inside the island O-point. Since this width is much smaller than the averaged width of the $n/m = 1/1$ island O-point, the finite Larmor radius effect can be ignored in the confinement of the titanium tracer ions inside the $n/m = 1/1$ island. As already confirmed in the LHD experiment, when the width of the vacuum $n/m = 1/1$ magnetic island exceeds the critical value (9 cm) [5], the radial electric field E_r is a negative in the half of the magnetic island towards the plasma edge and positive in the other half of the magnetic island away from the plasma edge. When the plasma is in the ion root, the space potential well is formed inside the $n/m = 1/1$ magnetic island O-point [5]. Since the plasma in our experiment is in the ion root (electron density and electron temperature at the island O-point are $1.1 \times 10^{19} \text{ m}^{-3}$ and 0.5 keV, respectively), this potential well would assist a good

confinement of the tracer impurity inside the $n/m = 1/1$ magnetic island O-point. This agrees well with the following observation; the highly-localized radiation from the titanium tracer ions inside the $n/m = 1/1$ magnetic island O-point remains stationary for a comparatively long time. In this paper, the qualitative behavior of the tracer impurity deposited inside the $n/m = 1/1$ magnetic island O-point is only presented. To obtain quantitative information on the impurity transport inside the magnetic island O-point is a future task. To this end, it is fundamental that the local impurity transport coefficients are evaluated both inside and outside the $n/m = 1/1$ magnetic island O-point, which would be difficult to perform. As a first step, appropriate optical filters for the XUV region, which dominates the radiation from the titanium tracer ions inside the $n/m = 1/1$ island O-point, will be attached to the AXUVD arrays for the near future experiments.

5. Conclusions

The local deposition of the tracer impurity inside the $n/m = 1/1$ magnetic island O-point, which is expanded by the external perturbation coils, has been achieved by means of TESPEL injection. The reconstructed 2D CT images for the chord-integrated AXUVD signals clearly show that the tracer impurity deposited inside the $n/m = 1/1$ magnetic island O-point remains stationary for a comparatively long time. This experimental result clearly indicates that the $n/m = 1/1$ static magnetic island O-point has good confinement capability for impurities as well as for heat and fueled particles.

Acknowledgement

The authors acknowledge all of the technical staff of NIFS for their excellent support. They also would like to thank Prof. O. Motojima (Director of NIFS) for his continuous encouragement. This work is partly supported by a Grant-in-Aid for Scientific Research (B) (No. 19340179) from the Japan Society for the Promotion of Science Japan and a budgetary Grant-in-Aid No. NIFS06KCHP008, NIFS08ULHH510 and NIFS08ULHH524 of the National Institute for Fusion Science.

- [1] Y. Kamada Plasma Phys. Control. Fusion **42** A65 (2000).
- [2] K. Ida *et al.*, Phys. Plasmas **11** 2551 (2004).
- [3] P. C. de Vries *et al.*, Plasma Phys. Control. Fusion **39** 439 (1997).
- [4] K. Tanaka *et al.*, Plasma Phys. Control. Fusion **44** A231 (2002).
- [5] K. Ida *et al.*, Phys. Rev. Lett. **88**, 015002-1 (2002).
- [6] B. P. van Milligen *et al.*, Nucl. Fusion **33** 1119 (1993).
- [7] A. Weller *et al.*, Phys. Rev. Lett. **59**, 2303 (1987).
- [8] R. D. Gill *et al.*, Nucl. Fusion **32** 723 (1992).
- [9] S. Inagaki *et al.*, Phys. Rev. Lett. **92**, 055002-1

- (2004).
- [10] K. Ida *et al.*, Plasma Phys. Control. Fusion **28** 895 (1986).
- [11] A. Komori *et al.*, Plasma Phys. Control. Fusion **42** 1165 (2000).
- [12] S. Sudo J. Plasma Fusion Res. **69** 1349 (1993).
- [13] N. Tamura *et al.*, J. Plasma Fusion Res. **78**, 837 (2002).
- [14] <http://www.ird-inc.com>
- [15] B.J. Peterson *et al.*, Plasma Phys. Control. Fusion **45** 1167 (2003).
- [16] C. Suzuki *et al.*, Rev. Sci. Instrum. **75** 4142 (2004).
- [17] D. S. Gray *et al.*, Rev. Sci. Instrum. **75** 4133 (2004).
- [18] A. W. Degeling *et al.*, Rev. Sci. Instrum. **75** 4139 (2004).
- [19] N. Tamura *et al.*, Rev. Sci. Instrum. **79** 10F541 (2008).
- [20] N. Iwama *et al.*, Appl. Phys. Lett. **54** 502 (1989).
- [21] M. Anton *et al.*, Plasma Phys. Control. Fusion **38** 1849 (1996).
- [22] Y. Liu *et al.*, Rev. Sci. Instrum. **77** 10F501 (2006).
- [23] R. A. Hulse, Nucl. Tech./ Fusion **3** 259 (1983).